Trees Talk Tremor—Wood Anatomy and $\delta^{13}C$ Content Reveal Contrasting Tree-Growth Responses to Earthquakes

Christian H. Mohr[1] , Michael Manga[2] , Gerhard Helle[3], Ingo Heinrich[3] , Laura Giese[4] , and Oliver Korup[1,5]

[1]University of Potsdam, Institute of Environmental Science and Geography, Potsdam, Germany, [2]Department of Earth and Planetary Science, University of California Berkeley, Berkeley, CA, USA, [3]GFZ German Research Centre for Geosciences, Potsdam, Germany, [4]German Federal Institute of Hydrology (BfG), Koblenz, Germany, [5]University of Potsdam, Institute of Geosciences, Potsdam, Germany

Abstract Large earthquakes can increase the amount of water feeding stream flows, raise groundwater levels, and thus grant plant roots more access to water in water-limited environments. We examine growth and photosynthetic responses of Pine plantations to the Maule M_w 8.8 earthquake in headwater catchments of Chile's Coastal Range. We combine high-resolution wood anatomic (lumen area) and biogeochemical ($\delta^{13}C$ of wood cellulose) proxies of daily to weekly tree growth sampled from trees on floodplains and close to ridge lines. We find that, immediately after the earthquake, at least two out of six tree trees on valley floors had increased lumen area and decreased $\delta^{13}C$, while trees on hillslopes had a reverse trend. Our results indicate a control of soil water on this response, largely consistent with models that predict how enhanced postseismic vertical soil permeability causes groundwater levels to rise on valley floors, but fall along the ridges. Statistical analysis with boosted regression trees indicates that streamflow discharge gained predictive importance for photosynthetic activity on the ridges, but lost importance on the valley floor after the earthquake. We infer that earthquakes may stimulate ecohydrological conditions favoring tree growth over days to weeks by triggering stomatal opening. The weak and short-lived signals that we identified, however, show that such responses are only valid under water-limited, rather than energy-limited tree, growth. Hence, dendrochronological studies targeted at annual resolution may overlook some earthquake effects on tree vitality.

Plain Language Summary Earthquakes deform and shake Earth's surface and the ground below. These changes may affect groundwater flow. Groundwater level may rise in the valley bottom and drop along higher elevated ridges. Trees depend on such groundwater resources, particularly in dry climates. Hence, we expect contrasting responses of trees after earthquakes: at higher elevations, access to groundwater may be impeded, but enabled in the valley bottoms. Thus, earthquake-enhanced tree growth should be pronounced only on valley floors, with opposite responses happening along ridges. We test this hypothesis in pine forest plantations that were affected by the 2010 Maule earthquake, Chile. We find that tree growth increased following the earthquake because of enhanced photosynthesis on valley floors, but decreased on upper hillslopes due to increased water stress. Overall, these responses are small but measurable. Our study is the first to combine state-of-the-art isotopic and wood anatomic proxies that we quantified at the cellular scale. Our results provide novel insights into the impacts of earthquakes on soil water and tree growth at an unprecedented daily to weekly resolution.

1. Introduction

Large prehistoric earthquakes are preserved in the geological record. Paleoseismology is the discipline concerned with reconstructing past earthquakes from this record, and mainly draws on offsets in fault scarps and river channels, deformed sediments, soil liquefaction, landslide and tsunami deposits (Ludwig, 2015), and archeological records (Nur, 2007). Biological archives recognize that the sudden subsidence of coasts during earthquakes may submerge and kill near-shore vegetation (Atwater & Yamaguchi, 1991), while shaking-induced damage to roots and damage from debris may suppress tree growth and be recorded in annual growth rings (Bekker, 2004; Jacoby et al., 1997; Lin & Lin, 1998; Meisling & Sieh, 1980; Page, 1970).

Tree growth can also be enhanced if neighboring and competing trees died due to earthquakes (Veblen et al., 1992), with larger individuals having the greatest survival potential (Allen et al., 2020). Earthquakes may elevate groundwater levels by increasing soil permeability and thus giving tree roots more access to water (Bekker et al., 2018; Mohr et al., 2015). Earthquakes as small as magnitude 4.6 have measurably affected tree growth (Sheppard & White, 1995). Trees offer some advantages over geological archives of past seismic shaking. Trees are abundant and may thus better constrain earthquake magnitude and location (Jacoby, 1997), and tree rings offer a yearly resolution that is more accurate than most geochronological tools (Jacoby et al., 1988; Sheppard & Jacoby, 1989). Indeed, most studies that searched for earthquake signals in trees analyzed the width of annual growth rings (Fu et al., 2020), though without considering possible effects of earthquake hydrology. Two common effects are falling groundwater levels along ridges or increased stream discharge (Rojstaczer et al., 1995; Wang et al., 2004) and can persist for weeks to months and modify regional water balances (Manga & Wang, 2015; Mohr et al., 2017). One dramatic biological manifestation of these hydrological changes was the contrasting response of trees to the M 8 New Madrid, USA, earthquakes in 1811. Lyell (1849) reported that "all the trees of a date prior to 1811, although standing erect and entire, are dead and leafless.... [on the] higher level plain, where the dead trees stand.... At the lower level are seen cypresses and cotton-wood, and other trees which delight in wet ground, all newer than 1812." (p. 1235). The growth surge in surviving bald cypress (*Taxodium distichum*) in the two years after the 1811 earthquakes was the largest ever recorded for this species in the southeastern United States (Arsdale et al., 1998).

The principal mechanisms invoked to explain hydrological changes following large earthquakes include pore-pressure response to seismic strain (Muir-Wood & King, 1993; Wakita, 1975), permeability changes caused by seismic waves (Elkhoury et al., 2006; Rojstaczer & Wolf, 1992; Wang et al., 2004), fluid migration along seismogenic dilatant cracks or crustal ruptures (Sibson & Rowland, 2003; Tsunogai & Wakita, 1996), or consolidation potentially up to liquefaction of sediments (Manga, 2001; Manga et al., 2003; Montgomery & Manga, 2003). Seismic shaking may also mobilize water from the unsaturated zone (Breen et al., 2020; Mohr et al., 2015). If tree growth is limited mainly by water (Babst et al., 2019), trees should in theory record hydrological responses to earthquakes by changing their growth rates.

Stable carbon isotope analysis has become an important tool to trace ecohydro-physiological processes in dendroecology (Gessler et al., 2014), as isotopic ratios in tree rings largely reflect conditions of the growing season (Reynolds-Henne et al., 2007). δ^{13}C measures the ratio of stable carbon isotopes ^{13}C–^{12}C (McCarroll & Loader, 2004). The fractionation of ^{13}C in wood occurs during photosynthetic diffusion and assimilation by the RuBisCo enzyme (Farquhar & Sharkey, 1982) because the heavier ^{13}C diffuses slower than ^{12}C (O'Leary, 1988), forming slightly stronger chemical bonds. This isotopic discrimination is recorded in the living wood (Dupouey et al., 1993; Helle & Schleser, 2004a, 2004b; Warren et al., 2001). A three-phase-model for broad-leaf trees (Helle & Schleser, 2004a) predicts (a) a lag effect of starch storage from previous years that raises δ^{13}C in early wood at the beginning of the vegetation period; (b) a decline δ^{13}C of during latewood formation; and (c) another increase in δ^{13}C at the end of the vegetation period during final latewood growth due to the same carbohydrate metabolic processes that form early wood. δ^{13}C is also sensitive to atmospheric CO_2 concentration as δ^{13}C discrimination in plants is related to the ratio of the CO_2 concentrations within the stomatal cavity and the ambient atmosphere (Farquhar et al., 1980; Keeling et al., 2017). For low temperatures, high water supply, or a combination of both, stomata apertures expand and RuBisCO preferentially assimilates ^{12}C from an abundant atmospheric pool, thus lowering δ^{13}C. In contrast, water stress, high temperatures or a combination of both, cause stomata apertures to decrease and reduce water loss through transpiration. Hence, photosynthetic diffusion is restricted and assimilation by RuBisCO may be less "picky" in terms of preferring ^{12}C, thus raising δ^{13}C (Helle & Schleser, 2004b). Wood anatomy is also sensitive to seasonal water supplies (Ziaco et al., 2016). Carvalho et al. (2015) found a high correlation between lumen area (LA) and soil moisture in water-limited Mediterranean conifer forests. Lumen is the membrane-defined intracellular space inside the elongated cells in the xylem of vascular plants called tracheids; lumen area refers to the cross-sectional surface (Ziaco et al., 2016). Assuming a sufficiently high number of tracheids formed per growing season and earthquake hydrological effects that persist for weeks to months (Manga & Wang, 2015), effects on tree growth should be recorded in wood anatomy. Seasonal patterns in δ^{13}C and lumen area thus reflect the interaction between seasonal micrometeorology, soil water, evapotranspiration, and tree growth (Gessler et al., 2014). By modulating access to shallow groundwater, earthquakes may cause favorable ecohydrological conditions and stimulate tree growth over days to weeks

by triggering stomatal opening. We expect such boosts, however, only under climatic conditions that favor tree growth, that is, water stress is relieved by providing additional water to trees. Thus, combining both wood anatomy and $\delta^{13}C$ could offer a proxy of tree growth and transpiration (Galle et al., 2010).

Summarizing this previous work, we hypothesize that strong ground shaking promotes tree growth close to streams, but hinders tree growth on hillslopes. We test whether rates of tree ring growth as recorded by wood anatomy and carbon isotopes responded to the M_w 8.8 2010 Maule earthquake, Chile. We then assess whether any such response outweighs other influences such as rainstorms (Carvalho et al., 2015). Finally, we discuss whether changes in tree ring growth recorded by individual cells can be a proxy for identifying past earthquakes on weekly to monthly time scales at unprecedented temporal resolution. To our knowledge, this is the first study of ecohydrological responses to earthquakes using stable isotopes and cell-level wood anatomy.

2. Study Area, Hydroclimatic Conditions, and Maule Earthquake

We study *Pinus radiata* D. Don trees in two headwater catchments of the Chilean coast range (Figure 1). Both catchments are in the rupture zone of the 2010 M_w 8.8 Maule earthquake that caused local peak ground velocities (PGV) of ~24 and 26 cm/s on the ridge and the valley bottom, respectively, for ~150 s (Moreno et al., 2010; Vigny et al., 2011). The earthquake-induced streamflow responses across south-central Chile yielded >1 km³ of excess discharge (Mohr et al., 2017). Groundwater models estimated an increase in evapotranspiration of 30%–60% for at least 5–10 days after the earthquake before new rainfall commenced (Mohr et al., 2015). Both study catchments, Pichún and San Antonio, have streamflow stage samplers, rain gauges, and air temperature loggers that were installed in April 2008 (Huber et al., 2010). Data from these instruments have been used to study hydrological and ecogeomorphic responses to the Maule earthquake (Mohr et al., 2012, 2015) and forestry operations (Barrientos et al., 2020; Mohr et al., 2013, 2014). Both catchments are geologically and topographically similar (Mohr et al., 2012). San Antonio covers 0.13 km² with elevations from 270 to 380 m asl and Pichún has 4.39 km² from 320 to 480 m asl (Figure 1). At the time of the earthquake, San Antonio had a mature (~25 years old) *Pinus radiata* D. Don plantation, whereas Pichún had two-year old *Eucalyptus* spp. seedlings with shallow (<1 m) roots. Deeper-rooting (>2 m) native species were restricted to 0.45 and 0.01 km² riparian buffers along the main streams, respectively (Mohr et al., 2012). *Pinus radiata* may produce >150 tracheids per growing season (Skene, 1969), which is high compared to other pine tree species (Carvalho et al., 2015). The higher the tracheid formation rate, the higher is the potential temporal resolution of wood anatomy.

The climate is Mediterranean (Csb) with a rainy season in the Austral winter and a hot, dry summer (Peel et al., 2007; Figure 2). The mean air temperature and rainfall during the growing season are 11.2 ± 0.55°C and 951 ± 205 mm, respectively (±1 standard deviation; Table S1). The growing seasons of 2011/12 and 2012/13 were extraordinarily dry as part of the multiyear Central Chile Mega Drought (Garreaud et al., 2020), which followed the wet El Niño winters of 2009/10 and 2010/11 (Kim et al., 2011). Soils (mostly Luvisols) and sediments >5-m thick in places (Mohr et al., 2012) may store water for trees even in drier conditions.

3. Data and Methods

We cored six *Pinus radiata* D. Don trees with a standard 40-cm Haglöfs increment corer of 4-mm inner diameter on February 16 and 17, 2014. We sampled all trees from upslope, downslope, and parallel to the contour line to account for reaction wood due to gravity (Du & Yamamoto, 2007). We chose sites on the valley-floor and hillslope ridges to check for topographic variations in tree responses to the earthquake (Figure 1), and considered several covariates to approximate subsurface hydrology, that is, the topographic wetness index (TWI), hillslope aspect, distance from the nearest stream, relative hillslope height, and the topographic position index (TPI) (Table 1, see Text S1). We ran all spatial computations in QGIS 3.2.2 and SAGA 2.3.2 (Figure 3 and Text S2). Additional information on sample preparation is in the Supporting Information S1.

Out of the 24 cores, we selected six cores that met the following criteria: (a) accurate dating and highly correlated measurements with an existing master reference curve; (b) distinct and straight tree ring borders; and (c) minimal number of features such as false, narrow, or missing rings. Four to six trees are sufficient
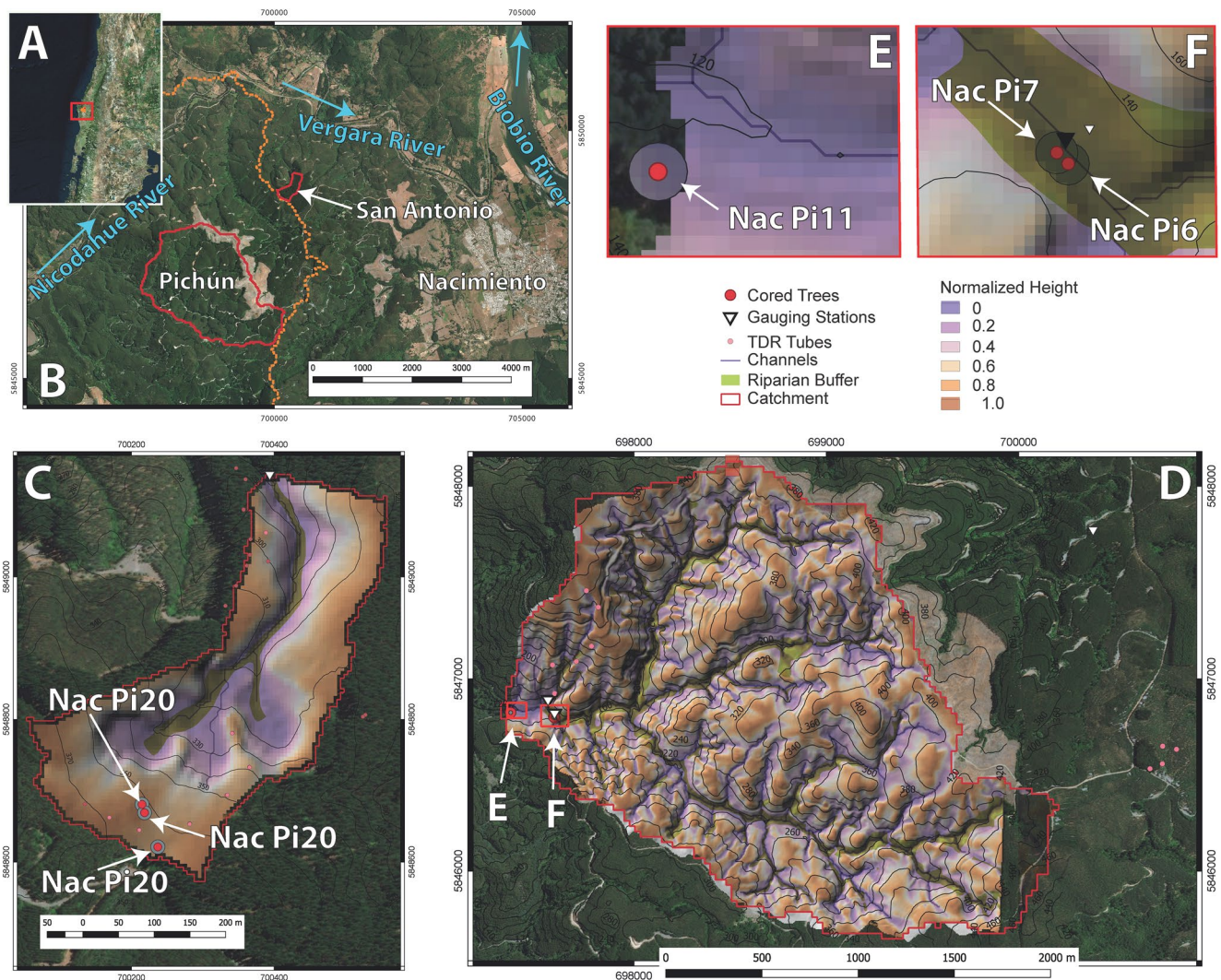
Figure 1. Study area. (a) Overview of study area in south-central Chile and (b) San Antonio and Pichún catchments: The Nicodahue River catchment is outlined by orange dots. Estimated relative slope positions for San Antonio (c) and Pichún (d, e, f); location of the cored trees is depicted by red circles NacPi refers to an abbreviation of "Nacimiento Pine;" pink circles are TDR-Trime Access tubes for soil-water monitoring and white triangles are streamflow gauges. Contour intervals are 10 and 20 m for San Antonio and Pichún, respectively. Basemaps (c) Bingmaps.

to approximate a "hypothetical perfect chronology" for isotope studies (Leavitt, 2010). We used data on streamflow, rainfall, temperature, and potential evapotranspiration (Hargreaves & Samani, 1985) from our monitoring campaigns in the catchments (Huber et al., 2010) (Figures 1 and 2) and from the CR2MET data for the Nicodahue catchment (#8362001) in the CAMEL-CL data set (Alvarez-Garreton et al., 2018). The Nicodahue catchment is the receiving basin of both Pichún and San Antonio catchments. All statistical *p*-values reported refer to the Wilcoxon rank-sum test. We performed all laboratory work at the dendro-chronological laboratory at GFZ Potsdam. We refer to the Text S2 for technical details.

3.1. Measurement of Wood Anatomic Parameters

We measured cell parameters using the confocal laser scanning technique (Liang et al., 2013). We quantified lumen area (LA), lumen diameter (LD), cell-wall thickness (CWT), and cell diameter (CD) using WinCell (Regent Instruments, Canada), a software developed for wood anatomy image analysis. We focus on lumen area, which is particularly sensitive to changes in soil water (Carvalho et al., 2015). We manually drew the tree ring boundaries using WinCell and tagged each tree ring with the corresponding growing season.
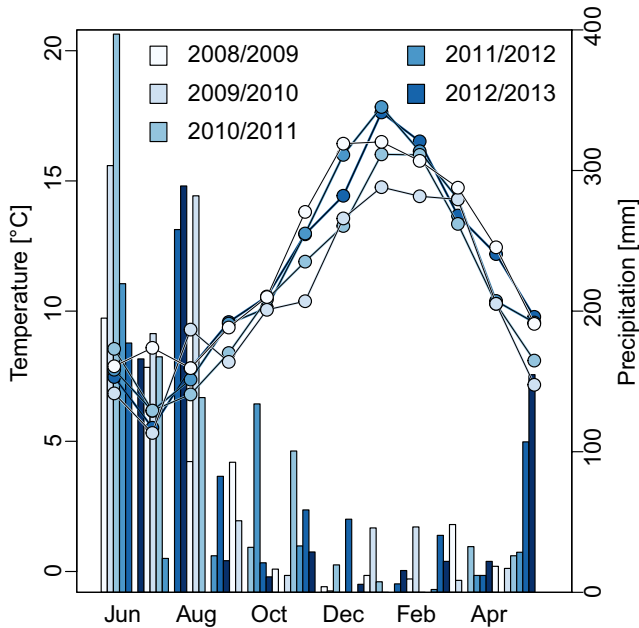
Figure 2. Monthly mean air temperature (°C) and precipitation (mm) during the growing seasons of 2008–2012; the catchment-averaged CR2MET data are from Nicodahue (#8362001, Figure 1) in the CAMELS-CL data set (Alvarez-Garreton et al., 2018).

WinCell connects two adjacent tree rings and creates "measurement regions" as the area between two subsequent rings. Within such regions, all tracheids were measured. Next, we manually define eight measurement paths within WinCell by selecting eight undisturbed cell rows that run in the radial direction from one tree ring boundary to the next. This way, we exceed the minimum number of six cell rows which are required according to Seo et al. (2014). One tracheid measurement path thus chronologically reflects the variations in cell growth from the beginning to the end of one growing season (Figure 3).

Tracheidograms show LA across the annual growth ring of a tree (Vaganov, 1990). Each cell line usually has an individual number of tracheids. To make tree rings comparable within a tree or from different trees, we normalized the number of cells per growing season along each path to the mean number of cells per hillslope position (Rossi et al., 2003), that is, ridge ($n = 159$) and valley bottom ($n = 108$). We calculated tracheidograms with the R package tgram (de la Cruz & De Soto, 2017).

3.2. δ^{13}C Sampling of Tree Rings

We performed high-resolution intraannual sampling by using an UV-Laser microdissection microscope (LMD 6, Leica Microsystems, Germany), largely following the protocol by Schollaen et al. (2015, 2017). We subdivided the annual rings into several subsections of ~100 µm in the radial direction marked by a pen screen. The number of subsections per ring was mostly >20 µm and varied depending on the tree-ring width (Table S1). We dissected every defined subsection with the UV-laser beam and collected the sample in a single tin capsule standing in a collection holder. We sealed the capsules and put them onto an autosampler of a Carlo Erba NA 1500 elemental analyzer coupled online to an Isoprime mass spectrometer (Elementar, Hanau, Germany). The isotopic composition of the carbon compound was expressed as relative differences of the ^{13}C/^{12}C ratio of tree material with respect to the Vienna Pee-Dee Belemnite (VPDB) standard. To differentiate between atmospheric δ^{13}C and δ^{13}C contained in tree organic matter, we use subscripts $_{atm}$ and $_{OM}$.

3.2.1. Modeling of Intercellular δ^{13}C and CO_2 Concentrations

We compared the measured $\delta^{13}C_{OM}$ values against modeled $\delta^{13}C_{OM}$ values. $\delta^{13}C_{OM}$ is the measured isotope fractionation of the cellulose samples. We rearranged the photosynthesis model by Farquhar et al. (1980)

$$\delta^{13}C_{OM} = \delta^{13}C_{atm} + \epsilon_D * \frac{(1 - c_i)}{c_{atm}} + \epsilon_C * \frac{c_i}{c_{atm}}, \tag{1}$$

Table 1
Topographic Characteristics for a 10-m Buffer Around the Sampled Cored Trees NacPi6–NacPi30

|	Sample ID					
	Valley bottom			Hillslope ridge		
Covariate	NacPi6	NacPi7	NacPi11	NacPi20	NacPi25	NacPi30
Altitude (m asl)	130.6 ± 1.6	129.9 ± 1.8	124.6 ± 1.4	361.9 ± 0.3	361.8 ± 0.9	362.6 ± 1.0
TWI	11.9 ± 3.6	11.0 ± 3.9	6.7 ± 1.3	7.5 ± 0.4	4.8 ± 0.2	4.7 ± 0.3
Aspect (°)	139 ± 126	118 ± 121	9 ± 5	83 ± 12	55 ± 2	63 ± 5
Distance from stream (m)	4.01	4.04	30.6	108.5	93.9	94.3
Relative hillslope height	0.01 ± 0.01	0.02 ± 0.01	0.19 ± 0.07	0.78 ± 0.01	0.90 ± 0.02	0.88 ± 0.04
TPI	−1.60 ± 0.25	−1.61 ± 0.28	−1.20+−0.15	0.11 ± 0.03	0.66 ± 0.04	0.59 ± 0.07
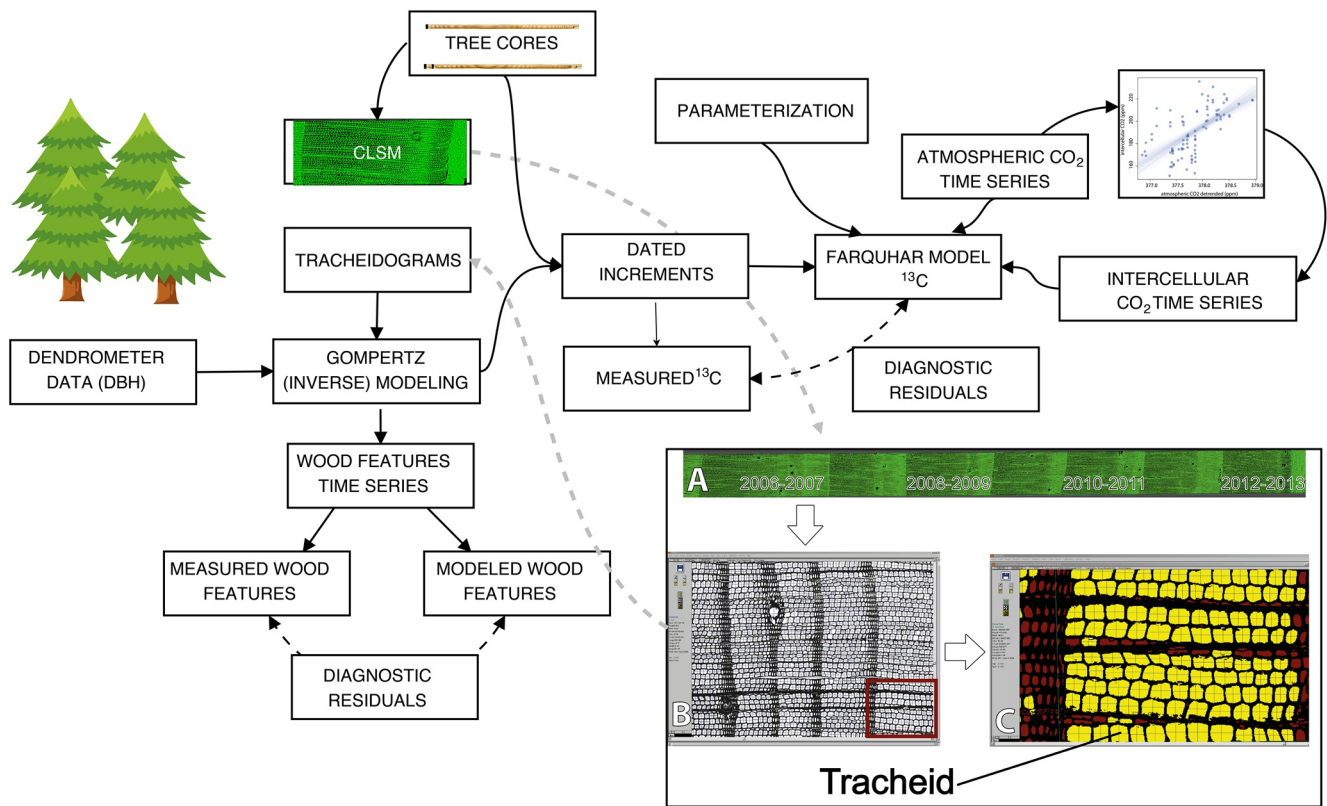
Figure 3. Overview of the workflow. Panels (a), (b), and (c) in the inset show a close-up of the working steps needed to obtain tracheidograms from the CLSM image (a), (b), and (c) show example screenshots of the WinCell application, with horizontal yellow bands illustrating single measurement paths.

to solve for leaf intercellular CO_2 concentrations (c_i) in the seasons 2008–2009 and 2011–2012 that we assumed are unaffected by the earthquake or starch storage (Helle & Schleser, 2004a)

$$c_i = \frac{c_{atm} * \left(\epsilon_D + \delta^{13}C_{atm} - \delta^{13}C_{OM}\right)}{\left(\epsilon_D - \epsilon_C\right)},$$

(2)

where c_{atm} is the atmospheric CO_2 concentration (ppm), ϵ_D is the fractionation for diffusion (−4.4‰), $\delta^{13}C_{atm}$ is atmospheric ^{13}C concentration (−8‰), and ϵ_C is fractionation at the CO_2 fixing enzyme, RuBisCo (−30‰); values for ϵ_D and $\delta^{13}C_{atm}$ are from Helle and Schleser (2004b). We used atmospheric CO_2 data from Baring Head, New Zealand (Keeling et al., 2001) to stand in for missing local or regional data. To correct for anthropogenic signals in atmospheric CO_2, we detrended c_{atm} by decomposing the c_{atm} data into seasonal, trend, and irregular components using R's loess function with default parameterization (R Core Team, 2020). We regressed the undisturbed c_i using a linear model of the detrended ambient atmospheric CO_2 concentration c_{atm} (Figure S2):

$$c_i = a + b\, c_{atm},$$

(3)

where a is the model intercept and b is the model slope. The fitted c_i feeds back into Equation 1 yielding

$$\delta^{13}C_{OM\_modeled} = \delta^{13}C_{atm} + \epsilon_D \frac{\left(1 - a\, b\, c_{atm}\right)}{c_{atm}} + \epsilon_C ab.$$

(4)

We assume that anomalies in $\delta^{13}C_{OM}$ caused by the earthquake are reflected in additional residuals (to the normally distributed noise) from predicted values. Thus, we use the model residuals as diagnostics of disturbance, following the disturbance hydrology approach by Buma and Livneh (2017). We assume that all residuals except the ones induced by the earthquake are normally distributed. We then compared the observed postseismic $\delta^{13}C_{OM}$ with the modeled values to calculate a Residual $\delta^{13}C_{OM}$-Signal (R$\delta^{13}C_{OM}$S)—the amount by which the observed $\delta^{13}C_{OM}$ differed from the modeled in the assumed absence of an earthquake disturbance at each time t

$$R\delta^{13}C_{OM}S = \delta^{13}C_{OM_{observed,t}} - \delta^{13}C_{OM_{predicted,t}} \tag{5}$$

$R\delta^{13}C_{OM}S$ approximates the role of earthquake disturbance in terms of the deviation from the expected $\delta^{13}C_{OM}$ time series. Our modified photosynthesis model is linear (Equation 4) even without using trend-adjusted CO_2 time series; thus, $R\delta^{13}C_{OM}S$ remains unchanged, though absolute residuals may change. Besides the modified Farquhar model, we calculated $R\delta^{13}C_{OM}S$ for a sinusoidal model, simulating a seasonal cycle of xylem growth and $\delta^{13}C_{OM}$ (King et al., 2013)

$$\delta^{13}C_{OM\_modeled} = \hat{X} \sin\left(\omega t + \varphi\right), \tag{6}$$

where $\hat{X}$ is the amplitude, ω is the angular frequency (rad/yr), and φ is the phase. We ran $n = 10,000$ MC models to account for uncertainties.

We also calculated $R\delta^{13}C_{OM}S$ against the arithmetic mean of all measurements per tree and growing season. This approach is widely used in dendroecology (Feng, 1998). To compare between trees and growing seasons, we standardized all residuals. We also calculated the residuals of modeled versus measured lumen area, that is, Residual Lumen Area Signal (RLAS). The increments cover intervals of different lengths depending on seasonal cell growth, and to make changes in $\delta^{13}C_{OM}$ comparable, we estimated daily rates of $\delta^{13}C_{OM}$ change with cubic smoothing splines with 10 degrees of freedom, following recommendations by Cantoni and Hastie (2001).

3.3. Timing of Cell Differentiation in Growing Cycle and Absolute Age Dating

We dated the tracheids and sample increments using dendrometer measurements at breast height (DBH) (courtesy of Oscar Maradones, Forestry SA Mininco). These measurements indicate that the growing season begins in June (Table S1). To estimate uncertainties regarding the timing of the growth measurements and the accuracy of DBH measurements, we ran $n = 10,000$ Monte-Carlo simulations of seasonal DBH growth. We assumed a uniform uncertainty of ± 10 days for the day of tracheid formation and a uniform DBH measurement accuracy of $\pm 1\%$. We estimated a date for each tracheid cell and $\delta^{13}C$-increment using the Gompertz growth model (Rossi et al., 2003), which is widely used for dating xylem growth in conifers, including *Pinus radiata* (Drew & Downes, 2018)

$$y = A \exp\left[-e^{\left(\beta - kt\right)}\right], \tag{7}$$

which we solved for the time of cell formation (t)

$$t = \frac{\beta - \ln\left[\ln\left(A + 1/y\right)\right]}{k}, \tag{8}$$

where y is the cumulative number of cells, A is the asymptotic maximum number of cells, β is a location parameter, k is a rate change parameter ($1/t$), and t is time in days starting on June 1 ($t = t_1$). To avoid infinite values, we fixed the upper asymptote at $A + 1$ (Rossi et al., 2003). We normalized the cumulative tree growth to establish a chronology for each growing season regardless of the number of tracheid cells (for wood anatomy) and the $\sim$100-μm-increments used for sampling $\delta^{13}C$. We dated the tree rings by measuring tree-ring width with WinDendro (Regent Instruments, Canada), and cross-dating all sampled cores with TsapWin (Rinntech, Heidelberg) and COFECHA (Holmes, 1983).

3.4. Boosted Regression Trees

We used Boosted regression trees (BRT) from the family of generalized boosted models (Elith et al., 2008; Hastie et al., 2009) to identify environmental controls on $\delta^{13}C_{OM}$ and lumen area other than seismic. This step highlights aseismic controls of tree growth among the tree cohorts and individuals. A BRT is an ensemble of decision trees, that is, a nonparametric model capable of handling large nonlinear, noisy, fragmented, or correlated multivariate data for classification and regression (Elith et al., 2008; Hastie et al., 2009). BRTs combine regression trees and boosting to build an ensemble of models. The hierarchical structure of BRTs means that the response to one input variable depends on residuals higher in the tree structure, so that interactions between predictors are modeled implicitly. Boosting is a sequential method for improving
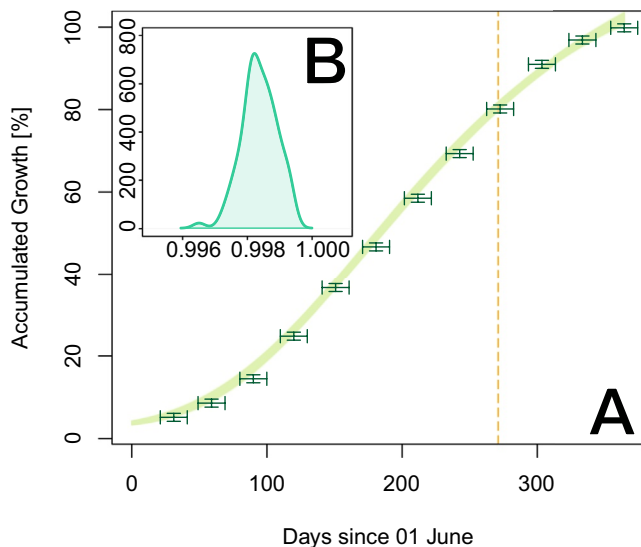
Figure 4. Cumulative tree growth per growing season. (a) Light green curves are $n = 10,000$ Monte-Carlo (MC) Gompertz model fits to the measured data (dark green). Dark green error bars encompass the measured monthly DBH growth with measurement errors (whiskers). The timing of the earthquake during the growing period is highlighted as the orange dashed line. (b) Distribution of the model fits (R^2 values) for the 10,000 MC models. The best-fit model parameters are $A = 132.0^{+5.03}/_{-4.18}$, $\beta = 1.54^{+0.06}/_{-0.06}$, and $\kappa = 0.009^{+0.001}/_{-0.001}$ (1/d) for our Gompertz growth model ($R^2 = 0.99$).

model accuracy, based on the idea that averaging the output of many poorly skilled models ("weak learners") can offer more accurate predictions ("strong learners") (Elith et al., 2008). The strategy is to sequentially train tree models on the residuals of their predecessors. The sequential fitting process builds on trees fitted previously, and increasingly focuses on the highest residuals to predict. This distinguishes the process from one where a single large tree is fitted to the data set (Hastie et al., 2009). Boosting minimizes the loss function by adding, at each step, a new tree that best reduces (or steps down the steepest gradient of) the loss function. Elith et al. (2008) pointed out that the stochastic model structure improves predictive performance. The variance of the final model is reduced by using only a random subset of data to fit each new tree (Friedman, 2002). The variance is controlled by defining the bag fraction that specifies the proportion of data to be selected at each step. A learning rate lr determines the contribution of each tree to the growing model, while tree complexity tc controls whether interactions are fitted. These two parameters then determine the number of trees (nt) required, with a lower lr requiring higher nt. In general smaller lr and larger nt are preferable (Elith et al., 2008). We used the R package gbm (Greenwell et al., 2020) and set the learning rate $lr = 0.001$ and tree complexity $tc = 5$, resulting in >3,000 trees, following recommendations by Elith et al. (2008); we set the bag fraction to 0.5. The model produces measures of variable importance based on the number of times a variable is selected for splitting, weighted by the resulting improvement to the model, and averaged over all trees (Friedman & Meulman, 2003). The relative importance of variables is normalized, with higher numbers indicating stronger influence on the response, thus augmenting a correlation matrix of linear dependence between predictors and response. The response variables are $\delta^{13}C_{OM}$ and mean lumen area (LA), whereas the predictors include antecedent mean solar radiation, mean air temperature, mean streamflow discharge and maximum, mean, and cumulative precipitation. The time windows encapsulated by each single measurement of LA and $\delta^{13}C_{OM}$ increments define the time window over which these antecedent conditions are integrated. For $\delta^{13}C_{OM}$, we integrated the data over 100-μm increments, and thus intervals ranging from days to weeks, depending on the time within the growing season. For the wood anatomy, we used the data per tree ring, that is, integrated over one growing season. Besides the topographic measures (Table 1) that we assume to remain unchanged during the growing season, our predictors also include tree and site-specific information, that is, the individual tree and slope position (ridge and valley bottom).

4. Results

4.1. Growth Modeling and Time of Cell Differentiation

Our field data indicate tree growth throughout the entire year, though growth rates decline during the winter months, potentially ceasing for a short period. The month of May contributes least to annual growth (1.4%) before growth reintensifies in June (2.5%) and July (3.3%) (Table S1). Based on the data we cannot exclude a short seasonal dormancy during May and June. For simplification, we use the term growing season here and define the growing season from June to May. The model overestimates accumulated growth during the early growing season, but more accurately fits growth toward its end, when the earthquake occurred (Figure 4).
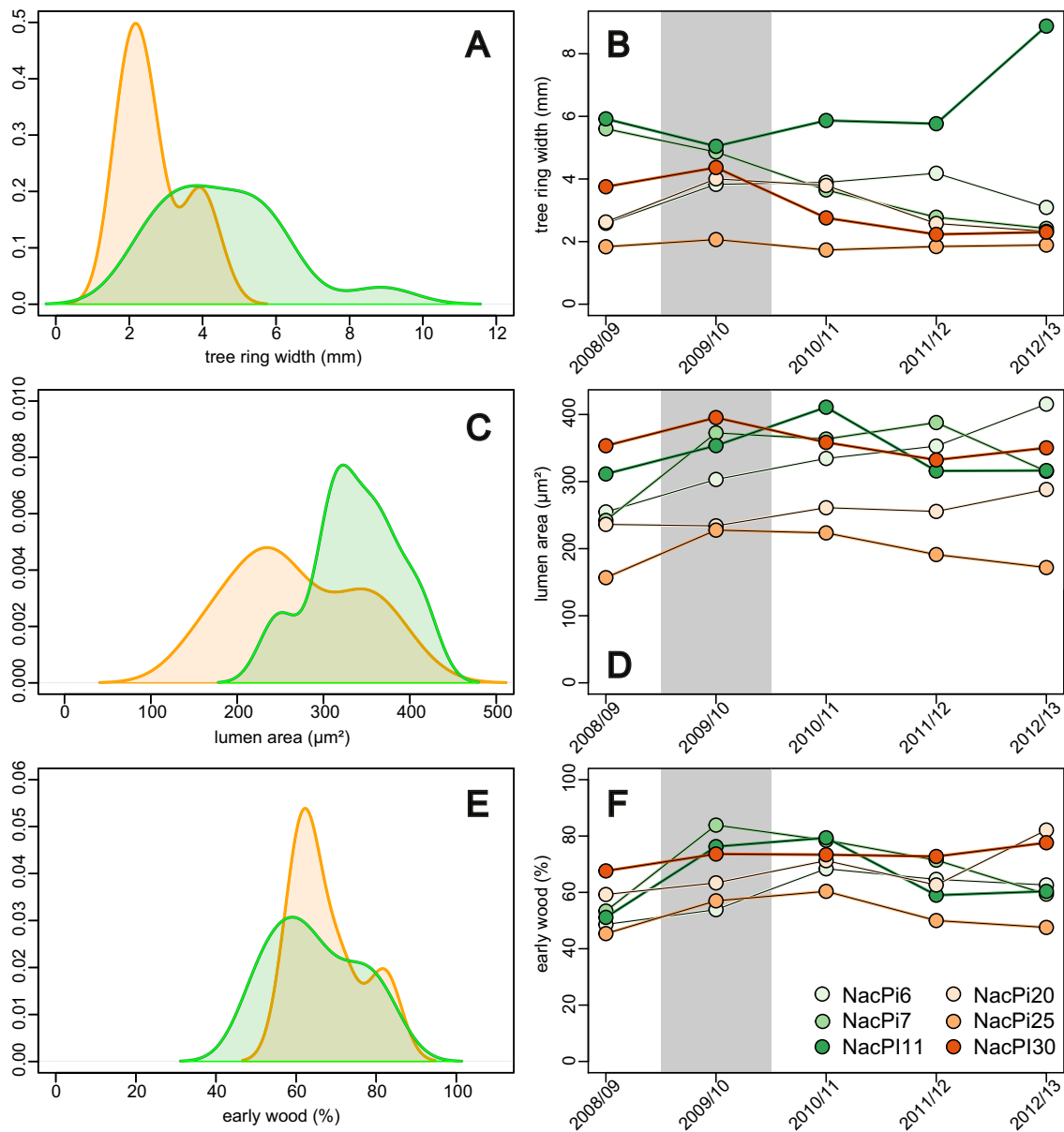
Figure 5. Summary of wood anatomic features. Density curves show (a) Tree-ring width (mm), (c) Lumen area (μm^2), and (e) Percentage of early wood grouped by hillslope ridges (orange) and valley bottom (green). Panels (b), (d), and (f) are the mean wood anatomic features per growing seasons. Gray shaded area marks the growing season in which the Maule earthquake occurred.

4.2. Wood Anatomy

4.2.1. Interannual Wood Anatomy

When averaged over all growing seasons from 2008 to 2013, tree-ring width (4.56 ± 1.71 and 2.67 ± 0.88 mm), lumen area (336.7 ± 50.4 and 269.0 ± 73.9 μm^2) and absolute early wood lumen area (412.9 ± 52.1 and 341.8 ± 64.6 μm^2) on valley floors exceed those on the hillslope ridge ($p \leq 0.01$) (Figures 5a and 5c). The percentage of early wood is indistinguishable ($p = 0.57$), with $67.7 \pm 9.2\%$ on the ridge and $64.7 \pm 11.1\%$ on the valley floor (Figure 5e).

On the ridge, the samples NacPi25 and NacPi30 (Table 1) have a similar temporal pattern (Figure 5b). Both samples show a moderate linear correlation ($r = 0.61$ and 0.58) between tree-ring width and lumen area. In contrast, the correlation among the valley-floor trees is negative ($r = -0.41$ to -0.62), and we note a strong
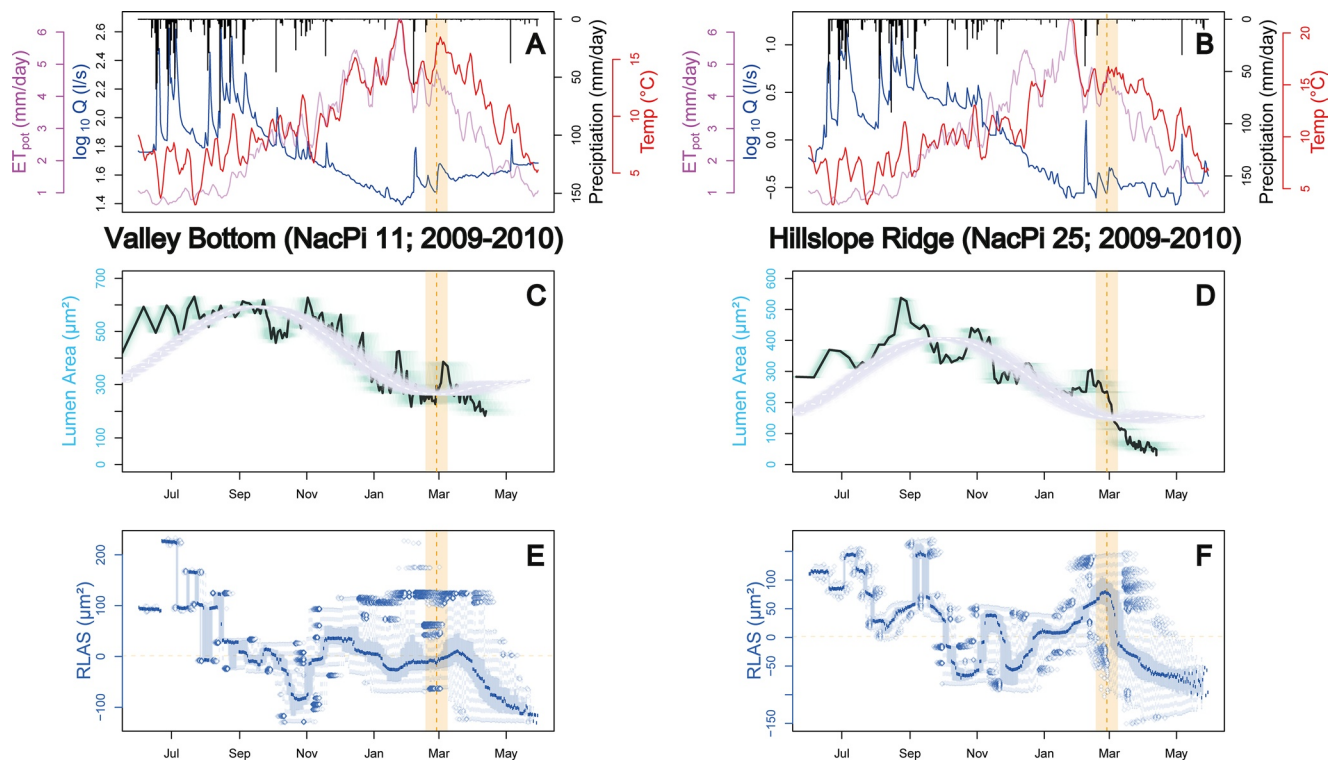
Figure 6. Wood anatomy of sampled trees on the valley floor (NacPi11 in panels (a), (c), (e)) and the hillslope ridge (NacPi25 in panels (b), (d), (e)) for the 2009–2010 growing season; streamflow discharge (in logarithmic scale) in blue, rainfall (black), and air temperature (red) measured in Pichún (a) and San Antonio (b); Potential evapotranspiration (red lines) in Nicodahue catchment (#8362001) from the CAMEL-CL data set (Alvarez-Garreton et al., 2018). The thick black curves are medians of $n = 10,000$ Monte-Carlo (MC)-modeled time series of lumen area (green array of curves) and the white dashed lines are the medians of $n = 10,000$ MC sinusoidal models for NacPi11 (c) and NacPi25 (d), respectively. The light blue boxplots are the RLAS (Residual Lumen Area Signal) binned to daily values (e), (f), with the medians in dark blue for NacPi11 (c) and NacPi25 (d), respectively. The orange bars and dashed lines mark the earthquake date ±10 days.

correlation between ring width and number of cells for both NacPi6 and NacPi11 ($r = 0.89$–0.99, see data in Table S7). Early wood hardly varied with time (Figure 5f and Table S7).

4.2.2. Intraannual Wood Anatomy

Our measurements identify anomalies in lumen area growth in at least two out of six samples, NacPi11 and NacPi25 (Figures 6c and 6d). These deviations from the sinusoidal model overlap with the timing of the Maule earthquake within dating resolution. NacPi11 had a positive deviation, with lumen area increasing from 250 to 390 μm^2 for about 1 month after the earthquake before returning to the pre-earthquake values (Figure 6c). The residuals are high compared to NacPi20 and NacPi30 (Figures S5 and S6), yet within the range of rainstorms in all growing seasons (Figure S11). Similar peaks in lumen area growth also happened in other growing seasons, for example, 2010–2011, tied to rainfall events at the beginning of the growing season (Figure S3). In contrast, rainfall was scarce in both catchments around the time of the Maule earthquake (Figures 6a and 6b), though lumen area does not scale with rainfall (Figure S12b).

Trees on the ridge had a decrease in lumen area immediately after the Maule earthquake, that was faster than predicted by the sinusoidal model (Figure 6d). The lumen area of NacPi25 decreased by 72% from 230 to 65 μm^2 between February 25 and March 18 (Figure 6d). A similar decrease also occurred in 2011, though stalled after rainfall and a rise in streamflow (Figure S4). Both NacPi20 and NacPi30 had similar, but smaller decreases (Figures S5 and S6).
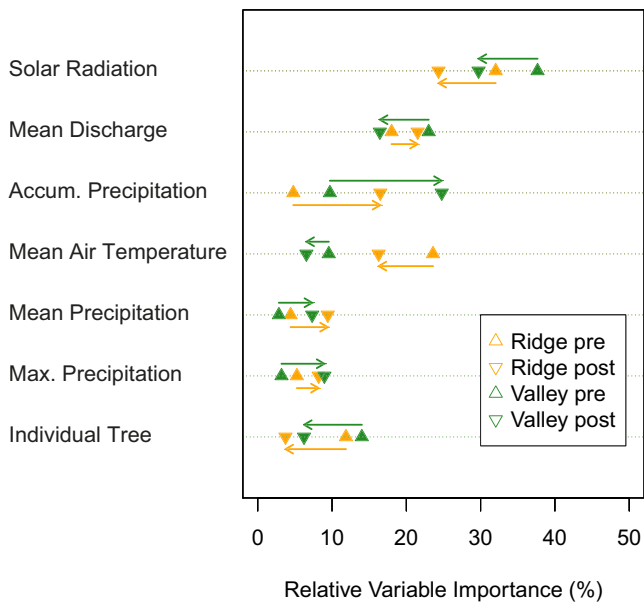
Figure 7. Relative variable importance of Generalized Boosted Regression Models of $\delta^{13}C_{OM}$ for hillslope ridges (orange) and valley floors (green) before and after the earthquake, respectively. The predictors solar radiation, mean temperature, mean discharge, and accumulated maximum and mean precipitation refer to intervals covered by a sample increment and thus vary; individual tree refers to location. The arrows show changes in variable importance after the earthquake on the ridge (orange) and the valley floor (green). See Table S3 for a complete list of relative variable importance and model fits.

4.3. $\delta^{13}C_{OM}$ Fractionation

From 1991 to 2012, the mean $\delta^{13}C_{OM}$ was higher in ridge trees ($-24.89 \pm 0.57‰$) than in those on the valley floor ($-25.18 \pm 0.72‰$; $p < 0.01$; Table S7). During this period, $\delta^{13}C_{OM}$ increased at $0.045‰$ year^{-1} for both topographic settings (Figure S8) with solar radiation consistently being the most important predictor (Figure 7). Accumulated rainfall was more important for $\delta^{13}C_{OM}$ after the earthquake compared to the pre-earthquake period. Vice versa, temperature was less important after the earthquake compared to the periods prior the earthquake. Postseismic streamflow was more important for $\delta^{13}C_{OM}$ on ridges than on the valley bottoms (Figure 7 and Table S3).

A correlation exercise reveals additional indications for underlying static, topographically determined hydroenvironmental controls. In essence, the wetter the site (see, e.g., TWI, TPI, normalized height, mean altitude, distance to the next stream, Figure S14), the higher is $\delta^{13}C_{OM}$. This scaling also applies for the wood anatomy. For example, TWI is positively correlated with $\delta^{13}C_{OM}$ (Figure S14).

After the earthquake, $\delta^{13}C_{OM}$ in NacPi11 decreased faster than our models predict, particularly that of the sinusoidal model (see a in Figure 8c), as the absolute (negative) model residuals switched from 0.24 (‰) on February 26 to -0.53 (‰) on the day of the earthquake and increased to -1.06 (‰) on March 29. A similar increase in residuals is also observed for both alternative modeling approaches; residuals are smallest for the sinusoidal model (Figure 8e). The estimated daily rates of $\delta^{13}C_{OM}$ largely remained unchanged ($p > 0.05$) (Figure 8c).

$\delta^{13}C_{OM}$ at NacPi20 also decreased from -24.04 (‰) on January 15 to a minimum of -27.07 (‰) of March 31. Amid this trend, a transient increase in the residuals may coincide with the timing of the earthquake (a in Figures 8d and 8f). Around the time of the earthquake, however, the rates fell slower when compared to a simple spline interpolation (b in Figure 8d). This small offset is in line with the observed transiently interrupted trend in $\delta^{13}C_{OM}$ decline toward the end of the growing season (Figure 8d). A transient increase in $\delta^{13}C_{OM}$ is also seen for NacPi30, even more pronounced in the model residuals (Figure S9).

5. Discussion

5.1. Site-Specific and Interannual Patterns of $\delta^{13}C_{OM}$ and Wood Anatomy

The increasing $\delta^{13}C_{OM}$ between 1991 and 2012 is consistent with an "age effect" of trees and increasing atmospheric CO_2 concentrations (Figure S8). Given tree ages of 21–26 years at the time of coring (Huber et al., 2010), the trees were at 70–90% of their maximum growth rates (Cerda Vargas & Nuñez Sandoval, 1996) (Figure S7), and likely in the thick of expanding their canopies. Adjusting for increased water-use efficiency in response to rising atmospheric CO_2 concentrations (Gessler et al., 2014), the residuals of our detrended photosynthesis model should increase with time, though this is not the case (Figure S8). The forests also remained undisturbed during the study period, so that changing shadow effects from neighboring trees (McCarroll & Loader, 2004, Mölder et al., 2011) are negligible.

In general, all dendroecological proxies indicate more favorable conditions for tree growth on the valley floor than on ridges, also if including elevation and discrimination rates of $\delta^{13}C_{OM}$ for *Pinus radiata* D. Don, $2.53‰$ km^{-1} (Warren et al., 2001). Elevation modulates carboxylation capacities and stomatal conductance (Qiang et al., 2003). Given mostly SSE-facing hillslopes and indistinguishable tree height distributions (Huber et al., 2010), we exclude higher irradiance along the valley bottom as a reason for this site-specific difference (Table S5). Instead, growth of *Pinus radiata* in Mediterranean areas such as south-central Chile is generally water-limited (Ojeda et al., 2018), thus following a temporal pattern determined by water supply
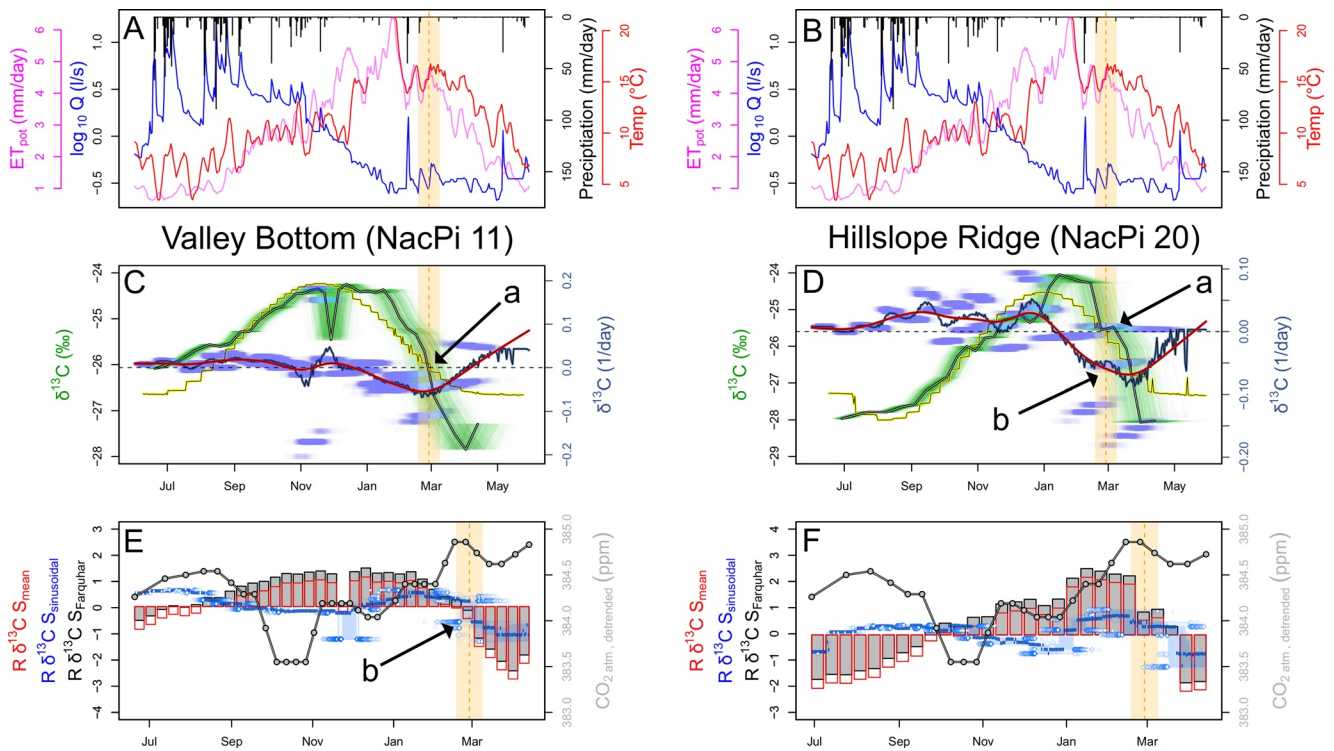
Figure 8. $\delta^{13}C_{OM}$ fractionation of NacPi11 (left) and NacPi20 (right) in the growing season 2009–2010. (a, b) Time series of discharge (on logarithmic scale) in blue, rainfall (black), air temperature (red), and potential evapotranspiration (pink). Data on streamflow discharge, rainfall, and air temperature from Pichún (a) and San Antonio (b) catchments, respectively; potential evapotranspiration from Nicodahue catchment (#8362001) of CAMEL-CL data (Alvarez-Garreton et al., 2018). The orange bars and dashed lines mark the earthquake date ±10 days. (c and d) The black curve is the median of all Monte-Carlo (MC)-modeled time series of $\delta^{13}C_{OM}$ ($n = 10,000$, green array of curves) of NacPi11 (c) and NacPi20 (d). Daily rates of $\delta^{13}C_{OM}$ change are violet points with violet solid line showing medians and red dashed line showing spline regression. The yellow curves are medians of $n = 10,000$ MC-based sinusoidal models per sampled cellulose increment. (e and f) Residual $\delta^{13}C_{OM}$ signals ($R\delta^{13}C_{OM}S$); gray and red bars are $\delta^{13}C_{OM}$ residuals of the Farquhar models and residuals between observed $\delta^{13}C_{OM}$ values and the annual mean, respectively. The blue boxplot time series are daily $\delta^{13}C_{OM}$ residuals of sinusoidal model. The gray dotted curves are detrended atmospheric CO_2 (ppm) measured at Baring Head, New Zealand (Keeling et al., 2001).

in the rainy season. We thus argue that tree growth (and photosynthesis) here is primarily controlled by water supply, given the strong correlations between $\delta^{13}C_{OM}$ and wood anatomic proxies with topographic proxies for soil-water availability. Consequently, the higher, farther from soil water, and drier a tree site is, the lower the $\delta^{13}C_{OM}$ and the more restricted is tree growth (Figure S14). This finding is consistent with observations for various environments (e.g., Bałazy et al., 2019; Jucker et al., 2018).

5.2. Potential Earthquake Effects on $\delta^{13}C_{OM}$ and Wood Anatomy

Regardless of topographic position, our intraannual measurements largely follow the three-phase $\delta^{13}C_{OM}$ sequence model for broad-leaf deciduous trees (Helle & Schleser, 2004a). We measured highest $\delta^{13}C_{OM}$ during periods of highest potential evapotranspiration during dry and hot summers (Figures 8c and 8d). Assuming above-average water supply during the 2009–2010 growing season (Figure 2 and Table S1), we expect below-average $\delta^{13}C_{OM}$ due to increased stomatal aperture and higher rates of photosynthesis (Helle & Schleser, 2004b) during the growing season of the Maule earthquake. Our observations of above-average wood anatomic features, that is, tree-ring width, number of cells, lumen area, and early wood formation support this notion. Especially lumen diameter of pines under water-limited conditions may correlate strongly with soil moisture (Carvalho et al., 2015).

The Maule earthquake occurred during latewood formation, so that the sudden changes in $\delta^{13}C_{OM}$ that deviate from the sinusoidal growth model around the time of the earthquake (e.g., Figure S9), are not storage effects limited to early wood (Helle & Schleser, 2004a). Instead, our observations are consistent with predicted earthquake-induced changes in groundwater and the vadose zone (Mohr et al., 2015).

Given the warm and dry conditions in summer 2010, we can assume narrow stomatal apertures and a slow decline of $\delta^{13}C_{OM}$ in the latewood of the 2009–2010 growing cycle. On the valley floor, the decrease in $\delta^{13}C_{OM}$ is faster than the modeled values (Figure 8c) immediately after the earthquake, thus suggesting enhanced photosynthesis following the Maule earthquake. In contrast, the abrupt, short-lived increase in $\delta^{13}C_{OM}$ at higher elevations (Figures 8c and 8d) implies limited photosynthesis and unfavorable growing conditions (Helle & Schleser, 2004b). The offset between the estimated daily rates of $\delta^{13}C_{OM}$ and the spline-interpolated values is, despite being small, "significant" and in line with this interpretation. Assuming that $\delta^{13}C_{OM}$ negatively scales with relative soil water (Dupouey et al., 1993), we explain these different responses with differences in soil-water availability following the earthquake.

Our wood anatomical results are in good agreement with this interpretation. In the water-limited Mediterranean climate, pine trees can plastically adjust their tracheid sizes to soil-water content. While enlarging the tracheids, water can only enter the expanding cell if the apoplastic water potential is higher than the symplastic water potential (Carvalho et al., 2015). Álvarez et al. (2012) and Ojeda et al. (2018) reported highly variable, rainfall-driven, growth in pine plantations within or close to the rupture zone of the Maule earthquake. However, we can exclude that rainfall raised the soil moisture on the valley floor, because conditions for several days prior to the earthquake were dry. Further, the sites are close together, have similar aspect, and thus likely receive similar amounts of rainfall.

Altogether, our data provide evidence for enhanced and reduced evapotranspiration on the valley bottom and ridge areas, respectively, likely caused by earthquake-triggered changes in soil-water availability. At a first glance, this finding is counter-intuitive as it suggests possible positive effects of earthquakes on tree growth as opposed to the many reports of negative effects (Fu et al., 2020; Lin & Lin, 1998; Meisling & Sieh, 1980). The contrasting responses on valley floors and ridges are more consistent with observations by Bekker et al. (2018), who found that tree rings were broader in a riparian zone compared to higher areas, likely driven by a rise in groundwater after the M6.9 1983 Borah Peak earthquake, Idaho. The peak ground velocity of >50−25 cm/s was similar for both the Borah and Maule earthquakes (Mohr et al., 2018; U.S. Geological Survey, 2021), both exceeding a threshold above which streamflow responses, and thus, potentially tree-growth responses, may be expected (Mohr et al., 2018).

The dendroecologic response on the hillslope ridge seems more uniform compared to the valley bottom (Figure 5b), perhaps reflecting groundwater topography. The local groundwater table is lower on hillslopes because the unconfined groundwater surface does not follow the surface topography. Hence, seismogenic lowering of the groundwater table can hardly make extremely dry soils much drier. On valley floors, however, even a small surplus of water may make a difference, thus stimulating the growth of water-starved trees. The subsurface is heterogeneous in soil hydrological terms due to previous rotations (Mohr et al., 2013). Hence, we cannot expect that all trees share a common, site-specific seismo-hydrological response. Some further possibilities for the differing growth responses to the Maule earthquake include death of neighboring trees due to forest management, wind throw (Buma & Johnson, 2015), or root damage by ground shaking (e.g., Lin & Lin, 1998; Meisling & Sieh, 1980; Spiecker, 2003). None of these anomalies were evident in the field, however.

The overall, relative effects of the Maule earthquake on wood isotopic fractionation and tree growth are small. For the valley bottom, the responses in $\delta^{13}C_{OM}$ and lumen area do not exceed the 78th and 83rd percentiles of the entire time series. Along the hillslope ridges, these responses are as small as the 13th percentile for $\delta^{13}C_{OM}$ and the 95th for the lumen area (Figure S11 and Table S8). Major rainstorms may have larger impact on the growth of these tress stands. Yet, a short-term positive earthquake effect on plant growth may potentially increase root cohesion immediately after the earthquake in low-lying areas (Tolorza et al., 2019), though seismic shaking may counteract this potentially stabilizing effect via higher soil-water content and/or ground acceleration (Sidle & Ochiai, 2006).

We argue that water stress around the time of an earthquake is required to detect hydrological effects of earthquakes in tree rings. Only under water-limited tree growth is additional water provided by seismo-hydrological processes likely to enhance root water uptake and eventually measurable changes in tree growth. Future research may want to examine the possibility of similar responses in other settings with prolonged dry seasons. Good candidates to test our hypothesis are earthquakes in California, for example, 2014 M6.6

South Napa or 1989 M6.9 Loma Prieta (Rojstaczer & Wolf, 1992; Wang & Manga, 2015). In contrast, the best studied earthquakes in terms of hydrological phenomena, the 1999 M7.7 Chi-Chi Earthquake in Taiwan (e.g., Wang et al., 2004, 2016), and the 2016 M7.0 Kumamoto earthquake in Japan (e.g., Hosono et al., 2020), are unlikely to be promising candidates because of the humid subtropical to tropical climates.

Several uncertainties remain part of our analysis. First, uncertainties in our dating procedure propagate trough time, thus increasing toward the end of the growing season, when the Maule earthquake occurred. This was a time when latewood formation reduced the temporal resolution. While this uncertainty is hard to quantify, we consider an interval of 21 days to be acceptable as it covers periods longer than a single cell needs to grow even at the end of the growing season. Thus, we are confident that our dating allows for sufficient interpretation. Second, a linear relationship between the leaf intercellular CO_2 concentrations and ambient atmospheric CO_2 concentration is simplified. Leaf intercellular CO_2 concentrations vary during a growing season (Gessler et al., 2014) following changes in temperature, and water vapor effects on stomata conductance and diffusivity (Tominaga et al., 2018). Yet, Moss and Rawlins (1963) reported a linear relationship with values close to our estimates. When comparing the residuals, our modified photosynthesis model performs (slightly) better than a simple, commonly applied approach of normalizing $\delta^{13}C_{OM}$ measurements (Feng, 1998). This supports the use of our modified Farquhar model together with our sinusoidal model to predict $\delta^{13}C_{OM}$ values with acceptable uncertainties.

6. Conclusions

High-resolution wood anatomy and isotopic data indicate possible dendrohydrological effects of the 2010 Maule earthquake on tree growth in two headwater catchments; these effects were varied, but likely discernable over weeks. The common dendrochronological practice restricted to the annual scale may therefore miss earthquakes or underestimate the area affected by a given earthquake. Our wood anatomy and biogeochemical data analyses indicate that postseismic changes in lumen area and $\delta^{13}C_{OM}$ reveal tree growth and photosynthetic responses to earthquakes. However, such responses likely only apply under water-limited conditions, that is, when earthquakes are capable to relief water stress by providing additional water to the trees. These circumstances need to be considered in sampling campaigns when considering tree coring in paleoseismology. The recorded response of tree growth to the Maule earthquake depends on the locations of the tree in the catchment, with enhanced growth along the valley floor but decreased growth along the ridges. Thus observed earthquake signals show in changes in $\delta^{13}C_{OM}$ and wood anatomical features, and lasted less than a year, unlike the longer-lived perturbation to tree growth documented in other studies based on tree-ring widths. Details in wood anatomy and isotopes might offer a tree-based approach for paleoseismology beyond simply considering width. Recognizing the subtle signals in the studied trees, however, benefited from known climatology, plausible parameterization of photosynthesis-models, and precipitation and temperature records.

Data Availability Statement

The dendroecological data sets used for this study may be accessed at Pangaea (https://doi.pangaea.de/10.1594/PANGAEA.935880). The hydroclimatic data are freely available as part of the CAMELS-CL data set by Alvarez-Garreton et al. (2018) (http://camels.cr2.cl/).

References

Allen, R. B., MacKenzie, D. I., Bellingham, P. J., Wiser, S. K., Arnst, E. A., Coomes, D. A., & Hurst, J. M. (2020). Tree survival and growth responses in the aftermath of a strong earthquake. *Journal of Ecology*, *108*(1), 107–121. https://doi.org/10.1111/1365-2745.13238

Álvarez, J., Allen, H. L., Albaugh, T. J., Stape, J. L., Bullock, B. P., & Song, C. (2012). Factors influencing the growth of radiata pine plantations in Chile. *Forestry*, *86*(1), 13–26. https://doi.org/10.1093/forestry/cps072

Alvarez-Garreton, C., Mendoza, P. A., Boisier, J. P., Addor, N., Galleguillos, M., Zambrano-Bigiarini, M., et al. (2018). The CAMELS-CL dataset: Catchment attributes and meteorology for large sample studies—Chile dataset. *Hydrology and Earth System Sciences Discussion*, 1–40. https://doi.org/10.5194/hess-2018-23

Arsdale, R. B. V., Stahle, D. W., Cleaveland, M. K., & Guccione, M. J. (1998). Earthquake signals in tree-ring data from the New Madrid seismic zone and implications for paleoseismicity. *Geology*, *26*(6), 515–518. https://doi.org/10.1130/0091-7613(1998)026<0515:esitrd>2.3.co;2

Atwater, B. F., & Yamaguchi, D. K. (1991). Sudden, probably coseismic submergence of Holocene trees and grass in coastal Washington State. *Geology*, *19*(7), 706–709. https://doi.org/10.1130/0091-7613(1991)019<0706:spcsoh>2.3.co;2

Babst, F., Bouriaud, O., Poulter, B., Trouet, V., Girardin, M. P., & Frank, D. C. (2019). Twentieth century redistribution in climatic drivers of global tree growth. *Science Advances*, *5*(1), eaat4313. https://doi.org/10.1126/sciadv.aat4313

Bałazy, R., Kamińska, A., Ciesielski, M., Socha, J., & Pierzchalski, M. (2019). Modeling the effect of environmental and topographic variables affecting the height increment of Norway spruce stands in mountainous conditions with the use of LiDAR data. *Remote Sensing*, *11*(20), 2407. https://doi.org/10.3390/rs11202407

Barrientos, G., Herrero, A., Iroumé, A., Mardones, O., & Batalla, R. J. (2020). Modelling the effects of changes in forest cover and climate on hydrology of headwater catchments in south-central Chile. *Water*, *12*, 1828. https://doi.org/10.3390/w12061828

Bekker, M., Metcalf, D. P., & Harley, G. (2018). Hydrology and hillslope processes explain spatial variation in tree-ring responses to the 1983 earthquake at Borah Peak, Idaho, USA. *Earth Surface Processes and Landforms*, *43*, 3074–3085. https://doi.org/10.1002/esp.4470

Bekker, M. F. (2004). Spatial variation in the response of tree rings to normal faulting during the Hebgen Lake Earthquake, Southwestern Montana, USA. *Dendrochronologia*, *22*(1), 53–59. https://doi.org/10.1016/j.dendro.2004.09.001

Breen, S. J., Zhang, Z., & Wang, C.-Y. (2020). Shaking water out of sands: An experimental study. *Water Resources Research*, *56*, e2020WR028153. https://doi.org/10.1029/2020WR028153

Buma, B., & Johnson, A. C. (2015). The role of windstorm exposure and yellow cedar decline on landslide susceptibility in southeast Alaskan temperate rainforests. *Geomorphology*, *228*, 504–511. https://doi.org/10.1016/j.geomorph.2014.10.014

Buma, B., & Livneh, B. (2017). Key landscape and biotic indicators of watersheds sensitivity to forest disturbance identified using remote sensing and historical hydrography data. *Environmental Research Letters*, *12*(7), 074028. https://doi.org/10.1088/1748-9326/aa7091

Cantoni, E., & Hastie, T. (2001). Degrees of freedom tests for smoothing splines. *Biometrika*, *89*(2), 251–263. https://doi.org/10.1093/biomet/89.2.251

Carvalho, A., Nabais, C., Vieira, J., Rossi, S., & Campelo, F. (2015). Plastic response of tracheids in pinus pinaster in a water-limited environment: Adjusting lumen size instead of wall thickness. *PLoS One*, *10*(8), e0136305. https://doi.org/10.1371/journal.pone.0136305

Cerda Vargas, I., & Nuñez Sandoval, R. (1996). *Appreciation of the Chilean forest resource: Plantations of Pinus radiata and Eucalyptus sp. 1985–1996*. Report FAO.

de la Cruz, M., & De Soto, L. (2017). Package "tgram". In *Functions to compute and plot tracheidograms*. https://doi.org/10.1139/x2011-2045>

Drew, D., & Downes, G. (2018). Growth at the microscale: Long term thinning effects on patterns and timing of intra-annual stem increment in radiata pine. *Forest Ecosystems*, *5*, 32. https://doi.org/10.1186/s40663-018-0153-z

Du, S., & Yamamoto, F. (2007). An overview of the biology of reaction wood formation. *Journal of Integrative Plant Biology*, *49*(2), 131–143. https://doi.org/10.1111/j.1744-7909.2007.00427.x

Dupouey, J.-L., Leavitt, S., Choisnel, E., & Jourdain, S. (1993). Modelling carbon isotope fractionation in tree rings based on effective evapotranspiration and soil water status. *Plant, Cell and Environment*, *16*(8), 939–947. https://doi.org/10.1111/j.1365-3040.1993.tb00517.x

Elith, J., Leathwick, J. R., & Hastie, T. (2008). A working guide to boosted regression trees. *Journal of Animal Ecology*, *77*(4), 802–813. https://doi.org/10.1111/j.1365-2656.2008.01390.x

Elkhoury, J. E., Brodsky, E. E., & Agnew, D. C. (2006). Seismic waves increase permeability. *Nature*, *441*(7097), 1135–1138. https://doi.org/10.1038/nature04798

Farquhar, G. D., & Sharkey, T. D. (1982). Stomatal conductance and photosynthesis. *Annual Review of Plant Physiology*, *33*(1), 317–345. https://doi.org/10.1146/annurev.pp.33.060182.001533

Farquhar, G. D., von Caemmerer, S., & Berry, J. A. (1980). A biochemical model of photosynthetic CO_2 assimilation in leaves of C3 species. *Planta*, *149*(1), 78–90. https://doi.org/10.1007/BF00386231

Feng, X. (1998). Long-term Ci/Ca response of trees in western North America to atmospheric CO_2 concentration derived from carbon isotope chronologies. *Oecologia*, *117*(1), 19–25. https://doi.org/10.1007/s004420050626

Friedman, J. H. (2002). Stochastic gradient boosting. *Computational Statistics and Data Analysis*, *38*(4), 367–378. https://doi.org/10.1016/s0167-9473(01)00065-2

Friedman, J. H., & Meulman, J. J. (2003). Multiple additive regression trees with application in epidemiology. *Statistics in Medicine*, *22*(9), 1365–1381. https://doi.org/10.1002/sim.1501

Fu, T., Liang, E., Lu, X., Gao, S., Zhang, L., Zhu, H., et al. (2020). Tree growth responses and resilience after the 1950-Zayu-Medog earthquake, southeast Tibetan Plateau. *Dendrochronologia*, *62*, 125724. https://doi.org/10.1016/j.dendro.2020.125724

Galle, A., Esper, J., Feller, U., Ribas-Carbo, M., & Fonti, P. (2010). Responses of wood anatomy and carbon isotope composition of *Quercus pubescens* saplings subjected to two consecutive years of summer drought. *Annals of Forest Science*, *67*(8), 809–809. https://doi.org/10.1051/forest/2010045

Garreaud, R. D., Boisier, J. P., Rondanelli, R., Montecinos, A., Sepúlveda, H. H., & Veloso-Aguila, D. (2020). The Central Chile Mega Drought (2010–2018): A climate dynamics perspective. *International Journal of Climatology*, *40*(1), 421–439. https://doi.org/10.1002/joc.6219

Gessler, A., Ferrio, J. P., Hommel, R., Treydte, K., Werner, R. A., & Monson, R. K. (2014). Stable isotopes in tree rings: Towards a mechanistic understanding of isotope fractionation and mixing processes from the leaves to the wood. *Tree Physiology*, *34*(8), 796–818. https://doi.org/10.1093/treephys/tpu040

Greenwell, B., Boehmke, B., & Cunningham, J. (2020). *gbm: Generalized boosted regression models*.

Hargreaves, G. H., & Samani, A. Z. (1985). Reference crop evapotranspiration from temperature. *Applied Engineering in Agriculture*, *1*(2), 96–99. https://doi.org/10.13031/2013.26773

Hastie, T., Tibshirani, R., & Freidman, J. (2009). *The elements of statistical learning—Data mining, inference, and prediction*. Springer.

Helle, G., & Schleser, G. H. (2004a). Beyond CO_2-fixation by Rubisco—An interpretation of $^{13}C/^{12}C$ variations in tree rings from novel intra-seasonal studies on broad-leaf trees. *Plant Cell and Environment*, *27*(3), 367–380. https://doi.org/10.1111/j.0016-8025.2003.01159.x

Helle, G., & Schleser, G. H. (2004b). Interpreting climate proxies from tree-rings. In H. Fischer, G. Floeser, T. Kumke, G. Lohmann, H. Miller, J. F. W. Negendank, & H. von Storch (Eds.), *Towards a synthesis of Holocene proxy data and climate models* (pp. 124–137). Springer. https://doi.org/10.1007/978-3-662-10313-5_8

Holmes, R. (1983). Computer-assisted quality control in tree-ring dating and measurement. *Tree-Ring Bulletin*, *43*, 69–78.

Hosono, T., Yamada, C., Manga, M., Wang, C.-Y., & Tanimizu, M. (2020). Stable isotopes show that earthquakes enhance permeability and release water from mountains. *Nature Communications*, *11*, 2776. https://doi.org/10.1038/s41467-020-16604-y

Huber, A., Iroumé, A., Mohr, C. H., & Frene, C. (2010). Effect of *Pinus radiata* and *Eucalyptus globulus* plantations on water resource in the Coastal Range of Biobio region, Chile. *Bosque*, *31*(3), 219–230. https://doi.org/10.4067/s0717-92002010000300006

Jacoby, G. C. (1997). Application of tree ring analysis to paleoseismology. *Reviews of Geophysics*, *35*(2), 109–124. https://doi.org/10.1029/96RG03526

Jacoby, G. C., Bunker, D. E., & Benson, B. E. (1997). Tree-ring evidence for an A.D. 1700 Cascadia earthquake in Washington and northern Oregon. *Geology*, *25*(11), 999–1002. https://doi.org/10.1130/0091-7613(1997)025<0999:trefaa>2.3.co;2

Jacoby, G. C., Sheppard, P. R., & Sieh, K. E. (1988). Irregular recurrence of large earthquakes along the San Andreas Fault: Evidence from trees. *Science*, *241*(4862), 196–199. https://doi.org/10.1126/science.241.4862.196

Jucker, T., Bongalov, B., Burslem, D. F. R. P., Nilus, R., Dalponte, M., Lewis, S. L., et al. (2018). Topography shapes the structure, composition and function of tropical forest landscapes. *Ecology Letters*, *21*(7), 989–1000. https://doi.org/10.1111/ele.12964

Keeling, C. D., Piper, S. C., Bacastow, R. B., Wahlen, M., Whorf, T. P., Heimann, M., & Meijer, H. A. (2001). *Exchanges of atmospheric CO2 and 13CO2 with the terrestrial biosphere and oceans from 1978 to 2000*. Scripps Institution of Oceanography.

Keeling, R. F., Graven, H. D., Welp, L. R., Resplandy, L., Bi, J., Piper, S. C., et al. (2017). Atmospheric evidence for a global secular increase in carbon isotopic discrimination of land photosynthesis. *Proceedings of the National Academy of Sciences of the United States of America*, *114*(39), 10361–10366. https://doi.org/10.1073/pnas.1619240114

Kim, D., Jang, Y.-S., Kim, D.-H., Kim, Y.-H., Watanabe, M., Jin, F.-F., & Kug, J.-S. (2011). El Niño-Southern Oscillation sensitivity to cumulus entrainment in a coupled general circulation model. *Journal of Geophysical Research*, *116*, D22112. https://doi.org/10.1029/2011JD016526

King, G., Fonti, P., Nievergelt, D., Büntgen, U., & Frank, D. (2013). Climatic drivers of hourly to yearly tree radius variations along a 6°C natural warming gradient. *Agricultural and Forest Meteorology*, *168*, 36–46. https://doi.org/10.1016/j.agrformet.2012.08.002

Leavitt, S. W. (2010). Tree-ring C-H-O isotope variability and sampling. *Science of the Total Environment*, *408*(22), 5244–5253. https://doi.org/10.1016/j.scitotenv.2010.07.057

Liang, W., Heinrich, I., Helle, G., Liñán, I. D., & Heinken, T. (2013). Applying CLSM to increment core surfaces for histometric analyses: A novel advance in quantitative wood anatomy. *Dendrochronologia*, *31*, 140–145. https://doi.org/10.1016/j.dendro.2021.09.002

Lin, C. W., & Lin, C. W. (1998). Tree damage and surface displacement—The 1931 M 8.0 Fuyun earthquake. *The Journal of Geology*, *106*, 751–758. https://doi.org/10.1086/516058

Ludwig, L. G. (2015). 4.21. Paleoseismology. In G. Schubert (Ed.), *Treatise on geophysics* (2nd ed., pp. 559–579). Elsevier. https://doi.org/10.1016/B978-0-444-53802-4.00088-9

Lyell, C. (1849). *A second visit to the United States of North America*. John Murray.

Manga, M. (2001). Origin of postseismic streamflow changes inferred from baseflow recession and magnitude-distance relations. *Geophysical Research Letters*, *28*(10), 2133–2136. https://doi.org/10.1029/2000GL012481

Manga, M., Brodsky, E. E., & Boone, M. (2003). Response of streamflow to multiple earthquakes. *Geophysical Research Letters*, *30*(5), 1214. https://doi.org/10.1029/2002GL016618

Manga, M., & Wang, C. Y. (2015). 4.12. Earthquake hydrology. In G. Schubert (Ed.), *Treatise on geophysics* (2nd ed., pp. 305–328). Elsevier. https://doi.org/10.1016/B978-0-444-53802-4.00082-8

McCarroll, D., & Loader, N. J. (2004). Stable isotopes in tree rings. *Quaternary Science Reviews*, *23*(7–8), 771–801. https://doi.org/10.1016/j.quascirev.2003.06.017

Meisling, K. E., & Sieh, K. E. (1980). Disturbance of trees by the 1857 Fort Tejon Earthquake, California. *Journal of Geophysical Research*, *85*(B6), 3225–3238. https://doi.org/10.1029/JB085iB06p03225

Mohr, C. H., Coppus, R., Iroumé, A., Huber, A., & Bronstert, A. (2013). Runoff generation and soil erosion processes after clear cutting. *Journal of Geophysical Research: Earth Surface*, *118*, 814–831. https://doi.org/10.1002/jgrf.20047

Mohr, C. H., Manga, M., & Wald, D. (2018). Stronger peak ground motion, beyond the threshold to initiate a response, does not lead to larger stream discharge responses to earthquakes. *Geophysical Research Letters*, *45*, 6523–6531. https://doi.org/10.1029/2018GL078621

Mohr, C. H., Manga, M., Wang, C.-Y., Kirchner, J. W., & Bronstert, A. (2015). Shaking water out of soil. *Geology*, *43*(3), 207–210. https://doi.org/10.1130/g36261.1

Mohr, C. H., Manga, M., Wang, C.-Y., & Korup, O. (2017). Regional changes in streamflow after a megathrust earthquake. *Earth and Planetary Science Letters*, *458*, 418–428. https://doi.org/10.1016/j.epsl.2016.11.013

Mohr, C. H., Montgomery, D. R., Huber, A., Bronstert, A., & Iroumé, A. (2012). Streamflow response in small upland catchments in the Chilean Coastal Range to the M-W 8.8 Maule earthquake on 27 February 2010. *Journal of Geophysical Research*, *117*, F02032. https://doi.org/10.1029/2011JF002138

Mohr, C. H., Zimmermann, A., Korup, O., Iroumé, A., Francke, T., & Bronstert, A. (2014). Seasonal logging, process response, and geomorphic work. *Earth Surface Dynamics*, *2*(1), 117–125. https://doi.org/10.5194/esurf-2-117-2014

Mölder, I., Leuschner, C., & Leuschner, H. H. (2011). $\delta^{13}C$ signature of tree rings and radial increment of *Fagus sylvatica* trees as dependent on tree neighborhood and climate. *Trees*, *25*(2), 215–229. https://doi.org/10.1007/s00468-010-0499-5

Montgomery, D. R., & Manga, M. (2003). Streamflow and water well responses to earthquakes. *Science*, *300*(5628), 2047–2049. https://doi.org/10.1126/science.1082980

Moreno, M., Rosenau, M., & Oncken, O. (2010). 2010 Maule earthquake slip correlates with pre-seismic locking of Andean subduction zone. *Nature*, *467*(7312), 198–202. https://doi.org/10.1038/nature09349

Moss, D. N., & Rawlins, S. L. (1963). Concentration of carbon dioxide inside leaves. *Nature*, *197*(4874), 1320–1321. https://doi.org/10.1038/1971320a0

Muir-Wood, R., & King, G. C. P. (1993). Hydrological signatures of earthquake strain. *Journal of Geophysical Research*, *98*(B12), 22035–22068. https://doi.org/10.1029/93JB02219

Nur, A. (2007). 4.22. Historical seismicity: Archaeoseismology. In G. Schubert (Ed.), *Treatise on geophysics* (2nd ed., pp. 581–592). Elsevier. https://doi.org/10.1016/B978-0-444-53802-4.00089-0

Ojeda, H., Rubilar, R. A., Montes, C., Cancino, J., & Espinosa, M. (2018). Leaf area and growth of Chilean radiata pine plantations after thinning across a water stress gradient. *New Zealand Journal of Forestry Science*, *48*(1), 10. https://doi.org/10.1186/s40490-018-0116-8

O'Leary, M. (1988). Carbon isotopes in photosynthesis. *Bioscience*, *38*(5), 328–336. https://doi.org/10.2307/1310735

Page, R. (1970). Dating episodes of faulting from tree rings—Effects of 1958 rupture of fairweather fault on tree growth. *The Geological Society of America Bulletin*, *81*(10), 3085. https://doi.org/10.1130/0016-7606(1970)81[3085:deofft]2.0.co;2

Peel, M. C., Finlayson, B. L., & McMahon, T. A. (2007). Updated world map of the Köppen-Geiger climate classification. *Hydrology and Earth System Sciences*, *11*(5), 1633–1644. https://doi.org/10.5194/hess-11-1633-2007

Qiang, W. Y., Wang, X. L., Chen, T., Feng, H. Y., An, L. Z., He, Y. Q., & Wang, G. (2003). Variations of stomatal density and carbon isotope values of Picea crassifolia at different altitudes in the Qilian Mountains, *Trees*, *17*, 258–262.

R Core Team. (2020). *R: A language and environment for statistical computing*. R Foundation for Statistical Computing.

Reynolds-Henne, C. E., Siegwolf, R. T. W., Treydte, K. S., Esper, J., Henne, S., & Saurer, M. (2007). Temporal stability of climate-isotope relationships in tree rings of oak and pine (Ticino, Switzerland). *Global Biogeochemical Cycles*, *21*, GB4009. https://doi.org/10.1029/2007GB002945

Rojstaczer, S., & Wolf, S. (1992). Permeability changes associated with large earthquakes—An example from Loma-prieta, California. *Geology*, *20*(3), 211–214. https://doi.org/10.1130/0091-7613(1992)020<0211:pcawle>2.3.co;2

Rojstaczer, S., Wolf, S., & Michel, R. (1995). Permeability enhancement in the shallow crust as a cause of earthquake-induced hydrological changes. *Nature*, *373*(6511), 237–239. https://doi.org/10.1038/373237a0

Rossi, S., Deslauriers, A., & Morin, H. (2003). Application of the Gompertz equation for the study of xylem cell development. *Dendrochronologia*, *21*(1), 33–39. https://doi.org/10.1078/1125-7865-00034

Schollaen, K., Baschek, H., Heinrich, I., & Helle, G. (2015). Technical note: An improved guideline for rapid and precise sample preparation of tree-ring stable isotope analysis. *Biogeosciences Discussion*, *12*, 11587–11623. https://doi.org/10.5194/bgd-12-11587-2015

Schollaen, K., Baschek, H., Heinrich, I., Slotta, F., Pauly, M., & Helle, G. (2017). A guideline for sample preparation in modern tree-ring stable isotope research. *Dendrochronologia*, *44*, 133–145. https://doi.org/10.1016/j.dendro.2017.05.002

Seo, J.-W., Smiljanić, M., & Wilmking, M. (2014). Optimizing cell-anatomical chronologies of *Scots pine* by stepwise increasing the number of radial tracheid rows included—Case study based on three Scandinavian sites. *Dendrochronologia*, *32*(3), 205–209. https://doi.org/10.1016/j.dendro.2014.02.002

Sheppard, P. R., & Jacoby, G. C. (1989). Application of tree-ring analysis to paleoseismology: Two case studies. *Geology*, *17*(3), 226–229. https://doi.org/10.1130/0091-7613(1989)017<0226:aotrat>2.3.co;2

Sheppard, P. R., & White, L. O. (1995). Tree-ring responses to the 1978 earthquake at Stephens Pass, northeastern California. *Geology*, *23*(2), 109–112. https://doi.org/10.1130/0091-7613(1995)023<0109:trrtte>2.3.co;2

Sibson, R. H., & Rowland, J. V. (2003). Stress, fluid pressure and structural permeability in seismogenic crust, North Island, New Zealand. *Geophysical Journal International*, *154*(2), 584–594. https://doi.org/10.1046/j.1365-246X.2003.01965.x

Sidle, R. C., & Ochiai, H. (2006). *Landslides. Processes, prediction, and land use*. American Geophysical Union. https://doi.org/10.1029/WM018

Skene, D. S. (1969). The period of time taken by cambial derivatives to grow and differentiate into tracheids in *Pinus radiata*: D. Don. *Annals of Botany*, *33*(2), 253–262. https://doi.org/10.1093/oxfordjournals.aob.a084280

Spiecker, H. (2003). Silvicultural management in maintaining biodiversity and resistance of forests in Europe—Temperate zone. *Journal of Environmental Management*, *67*(1), 55–65. https://doi.org/10.1016/S0301-4797(02)00188-3

Tolorza, V., Mohr, C. H., Carretier, S., Serey, A., Sepúlveda, S. A., Tapia, J., & Pinto, L. (2019). Suspended sediments in Chilean rivers reveal low postseismic erosion after the Maule earthquake (Mw 8.8) during a severe drought. *Journal of Geophysical Research: Earth Surface*, *124*, 1378–1397. https://doi.org/10.1029/2018JF004766

Tominaga, J., Shimada, H., & Kawamitsu, Y. (2018). Direct measurement of intercellular CO_2 concentration in a gas-exchange system resolves overestimation using the standard method. *Journal of Experimental Botany*, *69*(8), 1981–1991. https://doi.org/10.1093/jxb/ery044

Tsunogai, U., & Wakita, H. (1996). Anomalous changes in groundwater chemistry possible precursors of the 1995 hyogo-ken nanbu earthquake, Japan. *Journal of Physics of the Earth*, *44*(4), 381–390. https://doi.org/10.4294/jpe1952.44.381

U.S. Geological Survey. (2021). *ShakeMap, M 6.9—The Borah Peak earthquake*. https://earthquake.usgs.gov/earthquakes/eventpage/usp0001zbv/shakemap/pgv

Vaganov, E. A. (1990). The tracheidogramm method in tree-ring analysis and its application. In E. R. Cook, & L. A. Kairiukstis (Eds.), *Methods of dendrochronology: Applications in the environmental sciences* (pp. 63–76). Springer.

Veblen, T. T., Kitzberger, T., & Lara, A. (1992). Disturbance and forest dynamics along a transect from Andean rain forest to Patagonian shrubland. *Journal of Vegetation Science*, *3*(4), 507–520. https://doi.org/10.2307/3235807

Vigny, C., Socquet, A., Peyrat, S., Ruegg, J. C., Metois, M., Madariaga, R., et al. (2011). The 2010 M(w) 8.8 Maule megathrust earthquake of central Chile, monitored by GPS. *Science*, *332*(6036), 1417–1421. https://doi.org/10.1126/science.1204132

Wakita, H. (1975). Water wells as possible indicators of tectonic strain. *Science*, *189*(4202), 553–555. https://doi.org/10.1126/science.189.4202.553

Wang, C.-Y., Liao, X., Wang, L.-P., Wang, C.-H., & Manga, M. (2016). Large earthquakes create vertical permeability by breaching aquitards. *Water Resources Research*, *52*, 5923–5937. https://doi.org/10.1002/2016WR018893

Wang, C.-Y., & Manga, M. (2015). New streams and springs after the 2014 Mw6.0 South Napa earthquake. *Nature Communications*, *6*, 7597. https://doi.org/10.1038/ncomms8597

Wang, C. Y., Wang, C. H., & Manga, M. (2004). Coseismic release of water from mountains: Evidence from the 1999 (M-W=7.5) Chi-Chi, Taiwan, earthquake. *Geology*, *32*(9), 769–772. https://doi.org/10.1130/g20753.1

Warren, C. R., McGrath, J. F., & Adams, M. A. (2001). Water availability and carbon isotope discrimination in conifers. *Oecologia*, *127*(4), 476–486. https://doi.org/10.1007/s004420000609

Ziaco, E., Biondi, F., & Heinrich, I. (2016). Wood cellular dendroclimatology: Testing new proxies in great basin bristlecone pine. *Frontiers of Plant Science*, *7*, 1602. https://doi.org/10.3389/fpls.2016.01602